ELSEVIER

Contents lists available at ScienceDirect

Nuclear Instruments and Methods in Physics Research A

journal homepage: www.elsevier.com/locate/nima



Particle identification with COMPASS RICH-1

P. Abbon ¹, M. Alexeev ^{a,1}, H. Angerer ^j, G. Baum ^b, R. Birsa ^p, P. Bordalo ^{h,2}, F. Bradamante ^o, A. Bressan ^o, M. Chiosso ^m, P. Ciliberti ^o, M. Colantoni ⁿ, T. Dafni ¹, S. Dalla Torre ^p, E. Delagnes ¹, O. Denisov ⁿ, H. Deschamps ¹, N. Dibiase ^m, V. Duic ^o, W. Eyrich ^e, A. Ferrero ^m, M. Finger ^k, M. Finger Jr. ^k, H. Fischer ^f, C. Franco ^h, S. Gerassimov ^j, M. Giorgi ^o, B. Gobbo ^p, R. Hagemann ^f, D. von Harrach ⁱ, F.H. Heinsius ^f, R. Joosten ^c, B. Ketzer ^j, V.N. Kolosov ^{d,3}, K. Königsmann ^f, I. Konorov ^j, D. Kramer ^g, F. Kunne ¹, A. Lehmann ^e, S. Levorato ^p, A. Maggiora ⁿ, A. Magnon ¹, A. Mann ^j, A. Martin ^o, G. Menon ^p, A. Mutter ^f, O. Nähle ^c, F. Nerling ^f, D. Neyret ¹, D. Panzieri ^a, S. Paul ^j, G. Pesaro ^{o,*}, C. Pizzolotto ^e, J. Polak ^{g,p}, P. Rebourgeard ¹, F. Robinet ¹, E. Rocco ^m, G. Sbrizzai ^o, P. Schiavon ^o, C. Schill ^f, P. Schoenmeier ^e, W. Schröder ^e, M. Slunecka ^k, F. Sozzi ^p, L. Steiger ^g, M. Sulc ^g, M. Svec ^g, S. Takekawa ^o, F. Tessarotto ^p, A. Teufel ^e, H. Wollny ^f

ARTICLE INFO

Article history:
Received 14 June 2010
Received in revised form
10 November 2010
Accepted 22 November 2010
Available online 2 December 2010

Keywords: RICH COMPASS Particle identification Likelihood algorithms

ABSTRACT

RICH-1 is a large size RICH detector in operation at the COMPASS experiment since 2001 and recently upgraded implementing a new photon detection system with increased performance.

A dedicated software package has been developed to perform RICH-1 data reduction, pattern recognition and particle identification as well as a number of accessory tasks for detector studies.

The software package, the algorithms implemented and the detector characterisation and performance are reported in detail.

© 2010 Elsevier B.V. All rights reserved.

1. Introduction

The COMPASS experiment [1–6] at CERN SPS is dedicated to hadron physics, in particular to the study of the nucleon spin structure with muon probe and of a variety of issues in the hadron spectroscopy

sector, measurements by means of hadron beams. Both topics of this two-fold research programme require robust hadron identification. In the COMPASS spectrometer [6], it is provided by a large size Cherenkov imaging counter, RICH-1, operated in its initial version since 2001 [7] and in its upgraded version characterised by a more powerful photon detection system since 2006 [8,9].

Hadron identification is a powerful tool for the experimental investigation of heavy quark spectroscopy [10,11] and RICH counters are since a long time standard components of experimental setups dedicated to these measurements. Cherenkov imaging counters have been introduced only recently in the experiments dedicated to deep

^a INFN, Sezione di Torino and University of East Piemonte, Alessandria, Italy

^b University of Bielefeld, Bielefeld, Germany

^c Universität Bonn, Helmholtz-Institut für Strahlen- und Kernphysik, Bonn, Germany

 $^{^{\}rm d}$ CERN, European Organization for Nuclear Research, Geneva, Switzerland

^e Universität Erlangen-Nürnberg, Physikalisches Institut, Erlangen, Germany

^f Universität Freiburg, Physikalisches Institut, Freiburg, Germany

g Technical University of Liberec, Liberec, Czech Republic

h LIP. Lisbon, Portugal

ⁱ Universität Mainz, Institut für Kernphysik, Mainz, Germany

^j Technische Universität München, Physik Department, Garching, Germany

k Charles University, Prague, Czech Republic and JINR, Dubna, Russia

¹ CEA Saclay, DSM/DAPNIA, Gif-sur-Yvette, France

^m INFN, Sezione di Torino and University of Torino, Torino, Italy

ⁿ INFN, Sezione di Torino, Torino, Italy

[°] INFN, Sezione di Trieste and University of Trieste, Valerio 2, 34127, Trieste, Italy

^p INFN, Sezione di Trieste, Trieste, Italy

^{*} Corresponding author. Tel.: +39 0405583385; fax: +39 0405583350. E-mail addresses: giulia.pesaro@cern.ch, giulia.pesaro@ts.infn.it (G. Pesaro).

¹ On leave from JINR, Dubna, Russia.

² Also at IST, Universidade Técnica de Lisboa, Lisbon, Portugal.

³ On leave from IHEP, Protvino, Russia.

inelastic scattering of polarised leptons off polarised nucleons, becoming essential tools for these physics studies [6,12].

This article is dedicated to the software package built for COMPASS RICH-1 data reduction in order to perform pattern recognition and Particle IDentification (PID), and to study the detector performance. The software tools had been developed for the initial version of the detector and have been modified for the upgraded detector version, keeping unchanged both the basic architecture and the core of the reconstruction algorithm. In the following, we describe the version in use for the upgraded detector.

A short description of RICH-1 is presented in Section 2. Sections 3–6 describe the software package and present a discussion of the algorithms employed. The major calibration studies are reported in Sections 7 and 8. PID efficiency and purity are provided in Section 9. The impact of RICH-1 information on COMPASS data analysis is outlined in Section 10. Conclusions are given in Section 11.

2. The RICH-1 detector

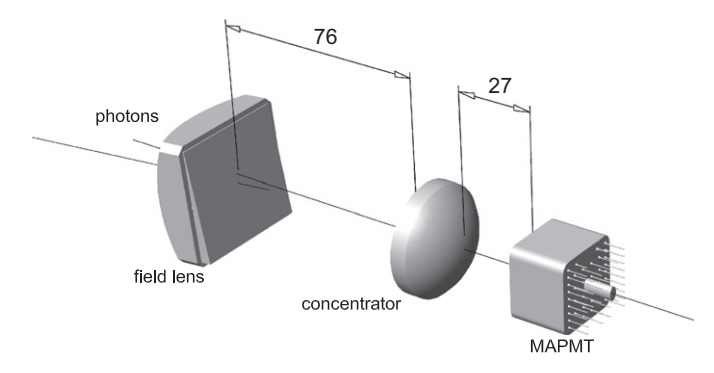
Fig. 1 provides a scheme of principle and an artist view of the detector. RICH-1 employs a gaseous radiator: particles cross 3 m of C_4F_{10} . The gas pressure and its transparency in a wide wavelength range down to the UV domain, required by the photon detectors used, are crucial parameters for the correct detector operation. The radiator gas system [13] allows to keep the gas pressure constant within 10 Pa, and ensures its transparency by continuous filtering: polluting contaminants, mainly oxygen and water vapour, that absorb far UV photons, are removed. Image focusing is obtained thanks to a 21 m² wall formed by a mosaic arrangement of 116 spherical UV mirror elements [14]. The wall consists of two (upper and lower) spherical surfaces (nominal radius of 6600 mm) with different orientation (Fig. 1). A stainless steel pipe (diameter 100 mm) with its axis coinciding with the beam axis is present inside the radiator volume: it intercepts the Cherenkov photons produced by the beam particles.

During the years 2001–2004, the photodetection in RICH-1 had been performed with MultiWire Proportional Chambers (MWPC) equipped with solid state CsI photocathodes [15]. One of the two cathode planes of the proportional chamber is a printed circuit board (PCB) segmented into $8\times 8~\text{mm}^2$ pads coated with a CsI film. The Cherenkov photons enter the chamber via a fused silica window and hit the photocathode PCB. The photoelectrons produced by the converted photons are multiplied in the MWPC. The detectors are operated at low gain (below 5×10^4), as imposed by the presence of the CsI photocathode. The first stage of the electronics read-out

system in use till 2004 [16] is characterised by a long integration time $(0.6~\mu s)$ related to the reduced gain: this results in an effective detector memory, limiting the RICH-1 performance in the COMPASS environment, where a high-rate uncorrelated background is present due to the large halo of the muon beam. Also, the base-line restoration time of the front-end in use till 2004 (about 3.5 μs) generates data acquisition dead-time. To overcome these limitations, and to face the higher rates foreseen for the COMPASS data taking from 2006 onwards, the RICH-1 detector has been upgraded.

The RICH-1 upgrade is two-fold. The peripheral regions (75% of the surface) are populated by the images produced by lower momentum hadrons, and experience a less severe level of the uncorrelated background. Here the photon detectors are unchanged; they are read out by a new system [17], based on the chip APV [18], with negligible dead-time and increased time resolution, obtained by measuring three amplitude samples on the raising edge of the signal.

The Cherenkov images produced by the high momentum particles are detected in the central photon detection area (25% of the surface), a region highly populated by the uncorrelated background images. These aspects require good resolution on the measured Cherenkov angle to rise towards momenta as high as possible the limit for hadron mass separation and fine time resolution to discriminate the uncorrelated background. This region is instrumented with a detection system based on MultiAnode PhotoMultiplier Tubes (MAPMT) [8] coupled to individual telescopes of fused silica lenses (a prismatic field lens followed by a concentrator lens) to enlarge the effective active area of the photon detectors (Fig. 2). The system allows to detect about four times more Cherenkov photons than in the peripheral detectors. The effective pad-size, resulting from the MAPMT pixel-size and the



 $\textbf{Fig. 2.} \ \ \text{Scheme of the two-lenses telescope system coupled to the MAPMT} (\ distances in mm).$

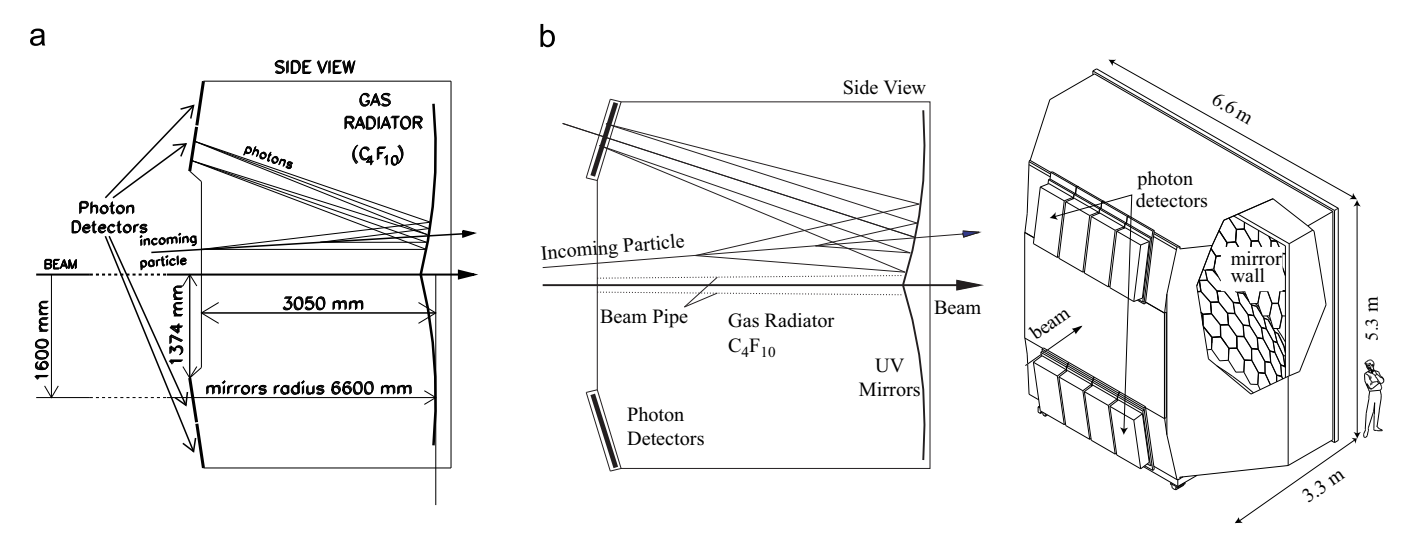


Fig. 1. A scheme of principle and an artist view of the COMPASS RICH-1 detector.

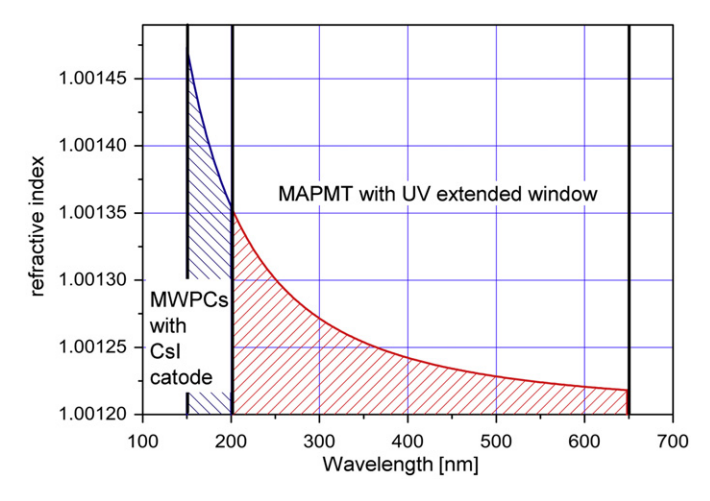


Fig. 3. Measured C_4F_{10} refractive index versus light wavelength at STP; data from Ref. [19]. The wavelength ranges of effective quantum efficiency for the MWPCs with CsI photocathodes and for MAPMTs with extended UV glass windows are indicated

lens telescope magnification, is about $12 \times 12 \text{ mm}^2$. These detectors, intrinsically fast and exhibiting sub-ns time resolution, are coupled to a read-out system based on high sensitivity amplifier/discriminators and fast TDCs, which fully exploits the fast photon detection characteristics of the new detection system [9].

The use of two different photon detector types employing different photoconverters results in the detection of photons in two different wavelength regions, as illustrated in Fig. 3. The resulting average values of the refractive index of the detected photons are also different, and in the following they are referred to as n_{UV} (MWPC) and n_{VS} (MAPMT). The maximum expected Cherenkov angle is about 55 mrad: this is the Cherenkov angle for photons at saturation, i.e. produced by a particle with $\beta \rightarrow 1$, detected in the outer part of the RICH; the Cherenkov angle for photons produced in the inner part of the RICH is smaller. Also the space resolution of the two detection systems is different, as indicated by the pad-size values quoted above.

3. Reconstruction tools

The reconstruction and analysis package for the RICH-1 detector is called RICHONE, which is part of CORAL, the COmpass Reconstruction and Analysis package [6].

3.1. The CORAL package

CORAL is an object oriented programme (written in C++), with modular architecture. CORAL can process both raw data as well as data produced by the Monte Carlo simulation software of COMPASS (COMGeant).

The most relevant tasks performed by CORAL are:

- the decoding of the data coming from all the detectors, to extract the addresses of the fired channels (*hits*), the signal amplitudes and the time information, when they are measured,
- the reconstruction of the particle trajectories (tracking), the momentum analysis of the charged particles, and the reconstruction of the interaction and decay vertices,
- the identification of the muons, using the information from the muon detectors,
- the analysis of the response of the hadronic and electromagnetic calorimeters,
- the RICH reconstruction and hadron PID, using the information from RICH-1.

The standard output of CORAL is a mini Data Summary Tape (mDST) containing all the relevant information for further physical analysis, including the PID from RICHONE.

Larger output files, storing more complete information, for instance all the RICH *hits*, can also be produced for detector calibration and apparatus studies.

3.2. The RICHONE package

RICHONE is a package performing both the standard PID and several accessory tasks, including tuning and calibrations.

The flow of RICHONE is based on three main steps (Fig. 4).

- The reconstructed coordinates measured by the RICH photon detectors are correlated to each particle trajectory reconstructed by CORAL; they are candidates for converted Cherenkov photons produced by the particle and are referred to as photons in the following.
- Using the *photons* and the particle momentum, provided by CORAL, as well as the measured refractive index, the value of a likelihood function is computed for each relevant mass hypothesis and for the hypothesis of absence of *signal* (the background hypothesis). This algorithm is the basis of the PID.
- In parallel, a pattern recognition is performed, to extract the Cherenkov photons emitted by the particle, on the basis of the expected ring image; it is so possible to cross-check the PID results and to perform internal consistency checks, as well as a fine tuning of the detector characteristic.

In the following the recognised patterns are referred to as rings.

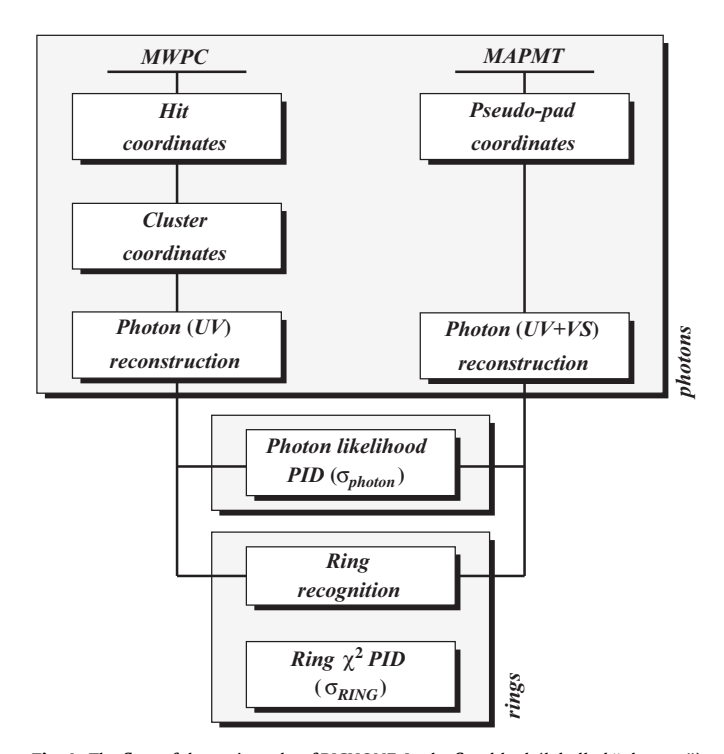


Fig. 4. The flow of the main tasks of RICHONE. In the first block (labelled "photons") the Cherenkov angles of the photon candidates are reconstructed, for both photon detector types (MAPMT and MWPC), decoding the measured information and taking into account the RICH-1 geometry. In the next step, the PID is performed, taking into account the experimental resolution on the photon Cherenkov angles. The next block (labelled "rings") includes accessory steps as the *ring* recognition procedure, intended mainly for the characterisation of several RICH-1 parameters or used as an alternative PID procedure and as an efficiency monitor.

4. The photon-to-particle correlation

4.1. The particle trajectories and momenta

PID is performed when the particle trajectory is within the geometrical acceptance at the RICH-1 entrance window and its momentum is within a given range (typically 1.8-180 GeV/c).

In CORAL a particle trajectory is defined giving its *helix* (position, direction and momentum). To reconstruct a trajectory inside RICH-1, a *helix* is computed at the RICH-1 entrance window; the trajectory is extrapolated inside the RICH-1 volume, taking into account the fringe field of the spectrometer magnet, located about 3 m upstream of RICH-1.

4.2. Hits and clusters on the photon detectors

The photon *hits* are measured on the RICH-1 photon detectors, together with either their time information for the MAPMTs or three signal amplitudes for the MWPCs.

The *hit* time information is used to reject out-of-time *photons*. The *hit* amplitudes are used to reduce the background both from out-of-time *photons* and from electronic noise (Section 2).

A converted photon can induce a signal on more than one adjacent MWPC pad; for this reason, a clustering procedure is used. After having found the pad with the maximum pulse height, the adjacent pads are included in the cluster if their pulse height is less than a percentage of this maximum value (60% for pads along the wire direction, 30% for those in the transverse direction). The impact position (*cluster*) is then evaluated as the mean of the *hit* positions, weighted with their pulse height. The average cluster multiplicity is 1.1. For the MAPMTs the probability to have correlated hits in adjacent

pixels is negligible [9]: no hit grouping is needed. For practical reasons the *hit* coordinate is projected onto the same plane of the MWPC pads, the pad plane. An incoming photon enters the lens telescope in front of a MAPMT at the surface of the field lens: the measured coordinates correspond to this entrance point. The lens surface is spherical and its distance to the pad plane varies between 0 and 5 mm. The orthogonal projection to the plane is performed, introducing a negligible distortion. The *hits* (MAPMT) and the *clusters* (MWPC) of a typical event are shown in Fig. 5. In the following, both MAPMT *hits* and MWPC *clusters* are referred to as *clusters*.

4.3. The photon reconstruction

The trajectory of a photon candidate is reconstructed from the position of its *cluster*, measured on the photon detector plane, and from its emission point [20]. This point is not known and it is assumed to be the average emission point of the detectable photons, calculated considering the particle trajectory inside the RICH radiator.

For each particle, all *clusters* present in a wide fiducial area of the photon detectors are correlated to the emission point. The reconstruction is carried out in the *photon plane*, the plane defined by the photon *cluster*, the photon emission point and the RICH-1 mirror centre of curvature; it contains the trajectory of the photon before and after its reflection.

The detailed geometry of RICH-1 is used for the angle reconstruction, including the measured radii and the positions of each mirror element of the mirror systems, and the fused silica window separating the radiator from the detectors.

The reconstructed photons are defined by giving their polar angles θ and φ in the particle reference system (PRS); PRS is defined with its *z*-axis along the particle trajectory and its *x*-axis lying in the

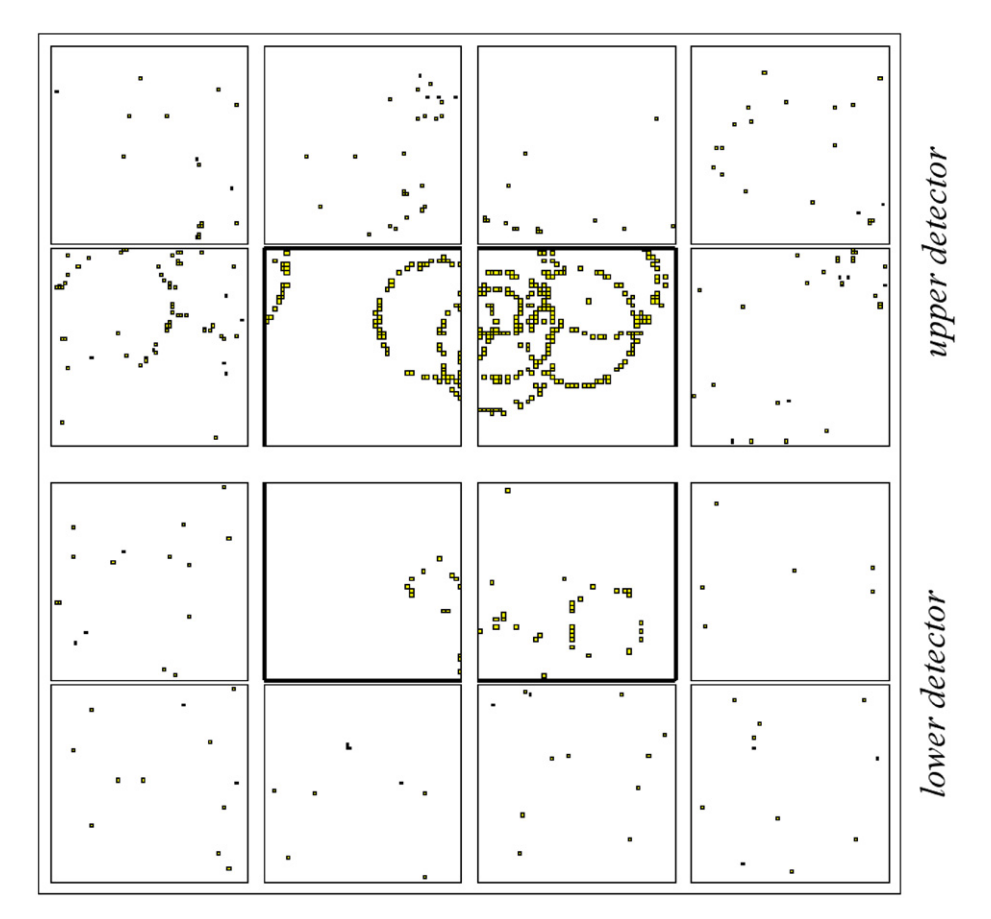


Fig. 5. A typical event display: many photon *rings* are visible. The 16 squares represent the photon detector frames. In the central part of the detectors, equipped with MAPMTs, there are more photons per *ring* and less background.

particle plane, namely the plane including the particle trajectory and its virtual reflection by the RICH-1 mirror. It is important to note that the reconstructed photons are relative to the considered particle and that this reconstruction is repeated for each particle in the event.

There are two different sources of discontinuity of the photon detection system due to the detector architecture (Section 2). The photon detectors form two sets separated in space (i), the upper and the lower detector sets. Correspondingly, the mirror wall is formed by two spherical surfaces with different orientations. Two types of photon detectors are used (ii). They have different space resolution and they detect photons in different wavelength ranges: the effective radiator refractive index is not the same for the two detector types. The reconstruction algorithm takes into account these discontinuities in a very natural way.

In particular, concerning discontinuity (i), for a particle at small polar angle (Θ_P) the Cherenkov photons do not hit all the same mirror surface: part of them hit the top (bottom) surface and they are reflected to the upper (lower) photon detector set. The expected ring pattern is then split between the two detectors; these images are referred to as *split rings*. Each photon candidate of a *split ring* is reconstructed with reference to its proper PRS; the resulting information is then taken into account altogether. For (ii), the reconstructed Cherenkov angle of the photons detected in one photon detector type is referred to the effective refractive index for that detector type. Then, the angle measured by MAPMTs are scaled to the corresponding MWPC angle, so that the resulting information from MAPMTs and MWPCs can be treated homogeneously: it is so possible to take into account all *photons* together, even when the

ring is not totally contained in a single detector type. Summarising, the whole available detector information is used in a unique process.

4.4. The corrections applied to the reconstructed photon angle

The lens telescope in front of the MAPMTs distorts the projection of the 4×4 array of the MAPMT channels on the pad plane. Namely, photons hitting the front lens surface at the same position but with different incident angles can activate different MAPMT channels and then they are projected back to the pad plane at a different position. The distortion is also dependent on the photon wavelength, which is unknown for each individual photon. To compute a set of corrections, ray tracing has been performed assuming the wavelength spectrum of the detected photons. The corrections obtained (Fig. 6) are functions of the photon direction and impact point; they are the weighted average of the wavelength dependent ones and they are applied to each photon after the first reconstruction step. The corrections are up to 4 mm in the worst case. The photon angle reconstruction is then iterated to account for the corrected *cluster* position.

4.5. The measured Cherenkov angle

For each particle the measured Cherenkov angle is determined from the reconstructed photon angles. Two algorithms are used providing two estimates of the angle: the likelihood-based method (Section 5.2) providing Θ_{ML} and the ring reconstruction method

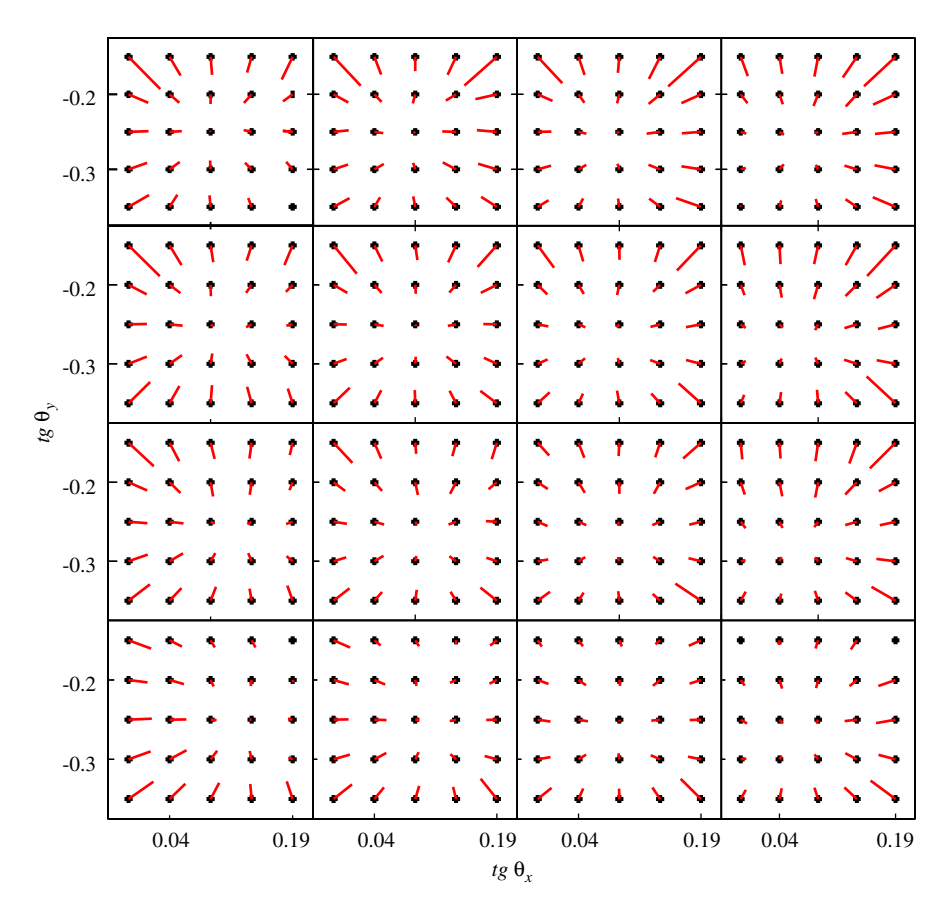


Fig. 6. A graphic representation of the optical corrections applied to take into account the presence of the lens system in front of each MAPMT. The 16 squares correspond to the 16 channels of each MAPMT; the grid of points inside each square correspond to different incidence angles onto the front lens surface $(tg\Theta_Y)$ versus $tg\Theta_X$; the line segments are the corrections to be applied, on the photon detector plane, to the *measured* position of the *pseudopad* corresponding to the MAPMT channel considered. The maximum correction is 4 mm.

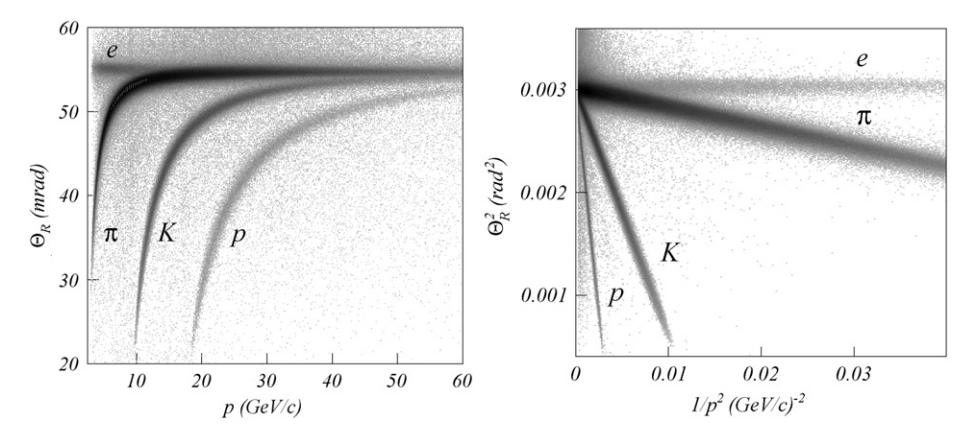


Fig. 7. The measured ring Cherenkov angle Θ_R versus the particle momentum p (left), and Θ_R^2 versus $1/p^2$ (right).

(Section 6), providing Θ_R . In Fig. 7 left, the measured ring Cherenkov angle Θ_R as a function of the particle momentum is shown. The Cherenkov thresholds for π , K, p are visible around 2.5, 9, 17 GeV/c respectively; above 50 GeV/c, the Cherenkov angles for each particle type reach the maximum value and the bands overlap. In Fig. 7 right, another relationship between the Cherenkov angle and the particle momentum is shown, which emphasises the small momentum region: Θ_R^2 as a function of $1/p^2$. In the small angle approximation, the relationship between these two variables is linear, with a slope proportional to the squared mass of the corresponding particle. The bands start at the Cherenkov threshold of the particles and have a common intercept corresponding to the maximum Cherenkov angle.

5. The Particle IDentification

5.1. The likelihood function

The PID is currently performed using the extended likelihood method [21]. For each accepted particle, the PID procedure is applied independently, disregarding the other particles of the same event.

The particle momentum p, provided by the tracking package, and the refractive index n of the radiator, provided independently (Section 7), are required to apply the PID algorithm.

Knowing p and n, for a particle of mass M, the expected Cherenkov emission angle Θ_M is computed from the Cherenkov equation:

$$\cos\Theta_{\rm M} = \frac{1}{n\beta} = \frac{\sqrt{p^2 + M^2}}{np}.$$
 (1)

The Cherenkov photons emitted by the considered particle are expected to have the same polar angle θ and an uniformly distributed azimuthal angle φ ; Cherenkov photons from the other particles in the event, *clusters* from out-of-time *hits* and from detector noise give origin to the *background*.

A fiducial region F is defined, keeping only photons with $\theta < \Theta_F$, fixed at 70 mrad, larger than the two maximum Cherenkov angles in the two detector types.

The extended likelihood function for each mass hypothesis *M* is written as (*N* is the number of photons)

$$\mathcal{L}_{M} = \exp[-(S_{M} + B)] \prod_{j=1}^{N} f_{M}(\theta_{j}, \varphi_{j})$$
(2)

where f_M takes into account that each photon can belong to the *signal* or to the *background*:

$$f_{M}(\theta, \varphi) = s_{M}(\theta, \varphi) + b$$

 $s_M(\theta, \varphi)$ and b do not need to be the normalised probabilities because an extended likelihood function is used.

In detail

$$s_{M}(\theta_{j}, \varphi_{j}) = \frac{S_{0}}{\sigma_{\theta j} \sqrt{2\pi}} \exp \left[-\frac{1}{2} \frac{(\theta_{j} - \Theta_{M})^{2}}{\sigma_{\theta j}^{2}} \right] \varepsilon_{D}(\theta_{j}, \varphi_{j})$$
(3)

where $S_0 = N_0 \sin^2 \Theta_M$ is the expected number of photons from the Frank-Tamm law. N_0 is the number of photons at saturation $(N_{\beta \to 1}/\sin^2\Theta_{M,\beta \to 1})$, tuned on data for each photon detector (Section 8.2). Θ_M is the Cherenkov angle expected for a particle of mass M and momentum p. $\sigma_{\theta j}$ is the single-photon resolution, calibrated on data (Section 8). $\varepsilon_D(\theta_j, \varphi_i)$ is the photon probability to reach the detectors, computed for each photon. The evaluation of $\varepsilon_D(\theta_i, \varphi_i)$ takes into account that the photons can be absorbed by the beam pipe (Section 2) or lost because of the holes between the mirror elements or because of the photon detector dead zones. b is computed from the average cluster distribution on the photon detectors, normalised to one event; it is a function of the photon position in the pad plane. It takes into account the physical background as well as the detector background, according to the experimental conditions. S_M and B in Eq. (2) are the expected number of signal and background photons respectively, and are obtained by integrating $s_M(\theta, \varphi)$ and b over F.

To compute the likelihood for the background hypothesis, it is assumed that $s_M(\theta_j, \varphi_i)$ is zero in Eq. (2).

In Eq. (2), the factor $\exp[-B]$ is common to the five mass hypotheses and to the background hypothesis and then irrelevant in the comparison among them; for this reason it is not taken into account.

Due to the different ranges of photon wavelength sensitivity of the two photon detector types, for a given particle mass, a $\Theta_M(VS)$ for the MAMPTs and a $\Theta_M(UV)$ for the MWPCs are predicted. In Eq. (3), Θ_M is then intended to be $\Theta_M(VS)$ or $\Theta_M(UV)$ according to the type of the detector hit by the jth photon.

5.2. The likelihood PID method

 \mathcal{L}_M is computed for five mass hypotheses (e, $\mu,$ K, $\pi,$ p) and for the background hypothesis.

The likelihood value is used for hypothesis testing; at the first order the maximum of the six \mathcal{L}_M values is assumed to correspond to the good hypothesis; more elaborate evaluations, based on the ratios of \mathcal{L}_M for different hypotheses, are also used in the analysis (Section 10).

In order to compare the likelihoods computed for different particles with different number of *photons*, namely with different degrees of freedom, the quantity \mathcal{L}_M is redefined as $\sqrt[N]{\mathcal{L}}_M$. This definition is intended to have a single \mathcal{L} distribution per particle type: it is so possible to tune consistently the cuts on this probability variable (Section 9). In the following \mathcal{L} refers to $\sqrt[N]{\mathcal{L}}$.

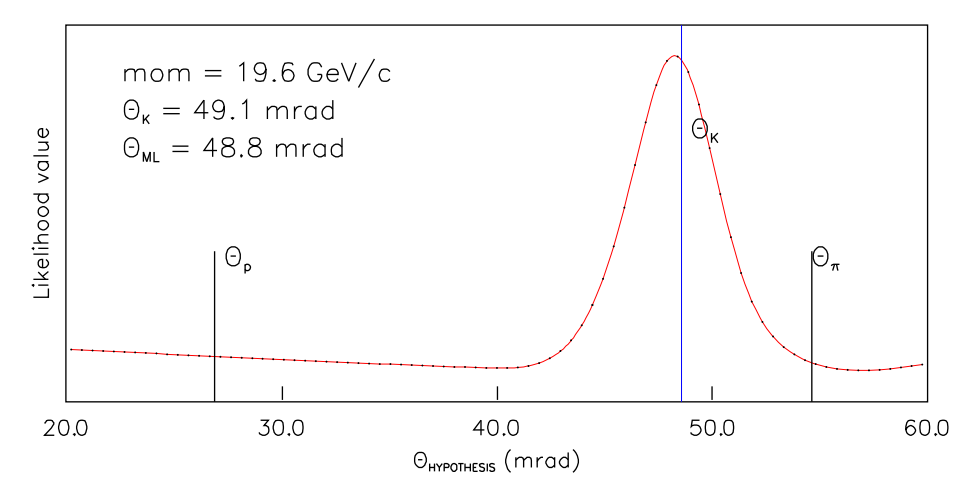


Fig. 8. The variation of the value of the likelihood as a function of the Cherenkov angle computed for a particle with 19.6 GeV/c momentum. The vertical lines correspond to the Cherenkov angles computed for the proton, kaon and pion masses. The PID suggests the kaon hypothesis. Θ_K does not coincide with Θ_{ML} , due to the experimental resolution on the measured *photon* angles.

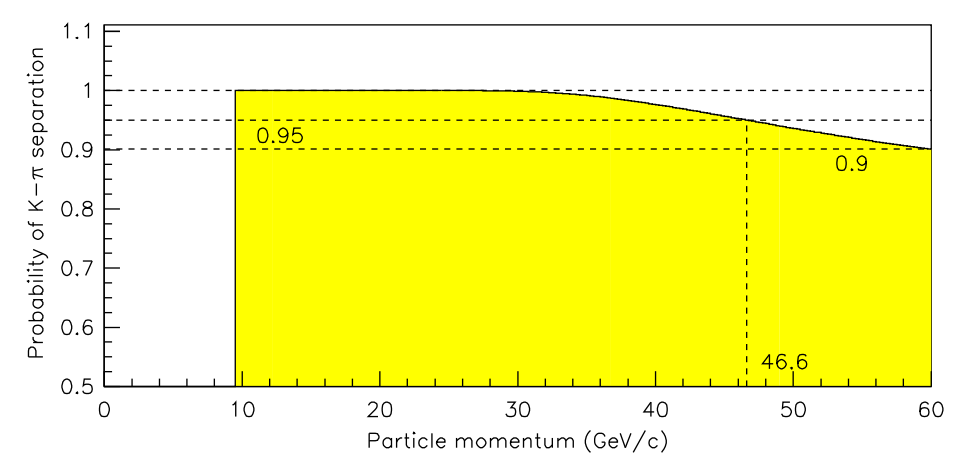


Fig. 9. Upper limit of the probability (solid line) of K $-\pi$ separation as a function of the particle momentum, taking into account the experimental resolution (details are given in the text). A probability of separation of 95% is achieved up to $P_{MAX} \simeq 45 \text{ GeV}/c$; for a 90% CL separation, $P_{MAX} \simeq 60 \cdot \text{GeV}/c$.

 \mathcal{L} is also computed as a function of Θ_M , assumed as a continuous parameter (Fig. 8); the value of Θ_M for which \mathcal{L}_M is maximum is taken as the maximum likelihood solution for the Cherenkov angle of the considered particle, Θ_{ML} .

5.3. The $K-\pi$ separation

The capability of a RICH counter to separate particles having different mass has been calculated from the resolution of the measured Cherenkov angle [20]. In this section we present a different calculation based on the likelihood function \mathcal{L} , and we apply it to the RICH-1 data.

The typical $\mathcal L$ experimental distribution exhibits a Gaussian-like peak, distorted by the contribution of the background; an example is given in Fig. 8. In the following discussion, we assume that the particle is a K. In general, Θ_{ML} does not coincide with Θ_K , due to the measurement resolution, $\sigma_{\Delta\Theta}$, which is the resolution of the measured Cherenkov angle provided by the maximum likelihood. $\sigma_{\Delta\Theta}$ is extracted from the data and, in RICH-1, it results almost independent from the momentum. The $\mathcal L$ peak distributes around Θ_K , fixed by kinematics, in an approximate Gaussian way. In the following we assume a perfect Gaussian distribution.

If Θ_K is larger than Θ_{ML} , $\mathcal{L}(\Theta_K)$ is always larger than $\mathcal{L}(\Theta_\pi)$, being Θ_π always larger than Θ_K . When Θ_K is smaller than Θ_{ML} by more

than one half of the difference $\Theta_{\pi}-\Theta_{K}$, $\mathcal{L}(\Theta_{K})$ is smaller than $\mathcal{L}(\Theta_{\pi})$, leading to a wrong PID; the probability of this wrong identification is calculated as the Gaussian probability of $0.5(\Theta_{\pi}-\Theta_{K})/\sigma_{\Delta\Theta}$. It is so possible to determine the maximum K momentum at which the K identification is still possible at a given confidence level (CL) (Fig. 9). In COMPASS RICH-1, assuming the measured experimental resolution, for a CL separation of 95% $P_{MAX} \simeq 45~\text{GeV}/c$; for a 90% CL separation, $P_{MAX} \simeq 60.~\text{GeV}/c$.

6. The ring recognition

The \emph{ring} recognition algorithm has been used mainly to tune the RICH response.

The aim is to select from all the reconstructed *photons* relative to a particle those which belong to the signal, namely the Cherenkov photons emitted by that particle (Fig. 10).

The distribution of the angle θ of all the *photons* relative to a particle up to Θ_F is scanned using a window of width $\Delta\theta$, counting the number of *photons* inside the window and looking for the value of θ for which the number of *photons* is maximum. Cherenkov photons are expected to have a Gaussian-like distribution around the value of the Cherenkov emission angle (Fig. 11). The window has typically a $\Delta\theta$ of $\pm 2\sigma_\theta$. We assume that most of the signal is

inside the window of maximum content and we take these *photons* to define the *ring*.

The ring angle Θ_R is then computed as the average of θ_j inside the window.

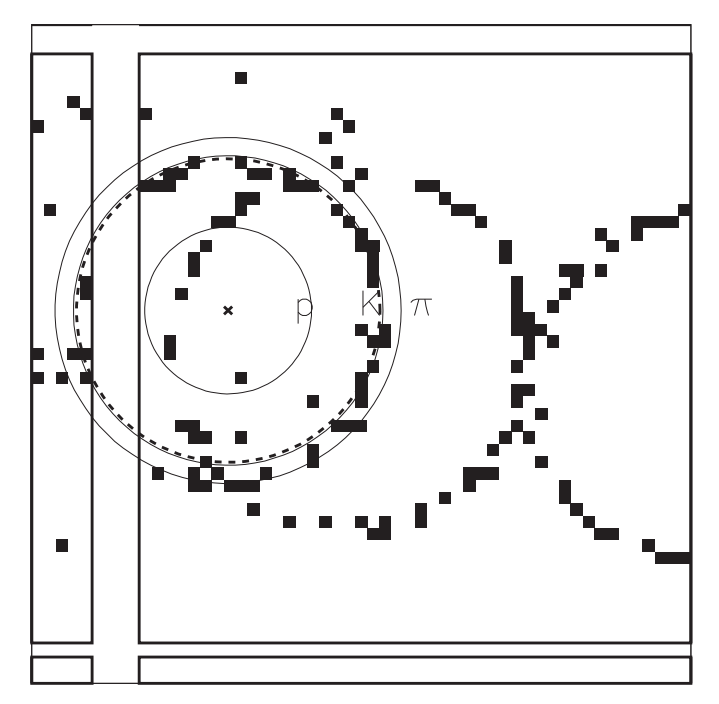


Fig. 10. A partial view of the central region of the photon detectors equipped with the MAPMT; the black squares are the *clusters*; at least three *rings* are visible. A single ring is analysed. The cross indicates where a particle with a momentum of 19.5 GeV/c should have hit the detector plane if reflected by the RICH mirrors; the three concentric circles (full lines) are the rings calculated in the hypothesis of proton (p), kaon (K) or pion (π) mass; the dotted circle is the reconstructed *ring*; the indication is in favour of the kaon hypothesis.

A ring χ^2 is computed, $\chi^2_R = \sum_j (\theta_j - \Theta_R)^2/\sigma^2_{\theta j}$, used as quality factor, as well as mass χ^2 , $\chi^2_M = \sum_j (\theta_j - \Theta_M)^2/\sigma^2_{\theta j}$, to be used as the test statistics in a simplified form of PID; note that the sum over the *photons* of the *ring* is without distinction between *signal* and *background*.

7. The radiator refractive index

The refractive index of the gaseous radiator depends on many parameters, mainly on the purity of the gas itself, the atmospheric pressure and the local temperature. Thus its value is time dependent. The measurement of the refractive index from the data is then necessary.

For each photon associated to a particle of measured momentum, the refractive index is computed, from the Cherenkov equation (Eq. (1)), assuming the π mass. The distribution of such values exhibits a Gaussian-like peak over a background. The peak is distorted mainly due to the contribution of the electrons present in the sample. The background level increases at high (n-1)-values, as expected on the base of geometrical considerations: in fact, the higher the (n-1)-value, the wider the portion of the detector surface contributing to the background. The overall background level is higher for the MAPMT data because those photodetectors equip the high occupancy region. The mean value of the Gaussian best fit of the peak is assumed as the index value (Fig. 12). The advantage of the method is that it has a minimal bias. More sophisticated distributions can be used, namely the distribution of Θ_R or distributions of θ for selected rings or for identified particles; they typically exhibit a cleaner peak, but they can suffer from biases due to the selection of the sample.

As described in Section 2, the data from MAPMTs and the data from MWPCs provide two different values of the refractive index, n_{VS} and n_{IIV} .

Note that high accuracy is needed: a Δn of 10^{-5} with respect to a reference value of $n \simeq 1.00150$ corresponds to a $\Delta \theta$ of the order of 0.2 mrad.

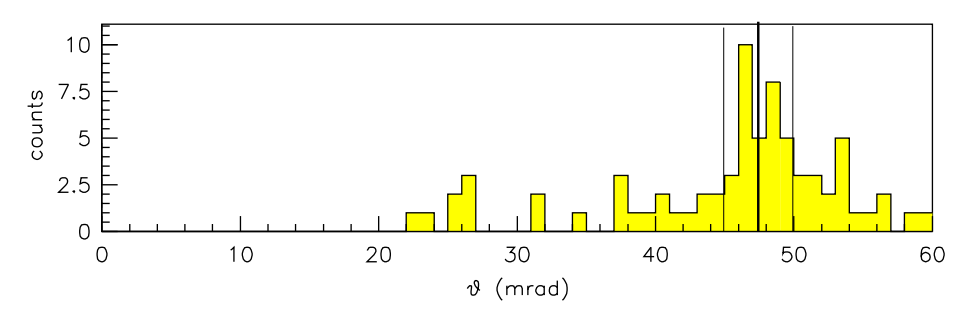


Fig. 11. The distribution of the polar angles of the *photons* with respect to the direction of the particle of the example in Fig. 10; the left and the right vertical lines define the *ring* search window; the window is set at the position where the number of counts (*photons*) inside it is maximum and the central line corresponds to the reconstructed *ring* angle.

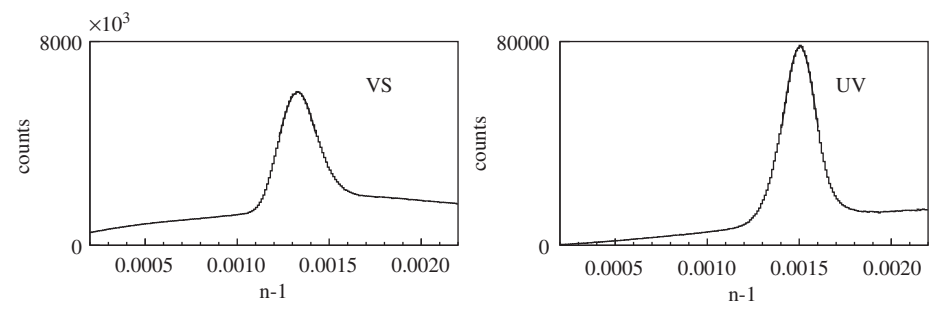


Fig. 12. Distribution of the refractive index value calculated for the detected photons. Left: MAPMT data, visible and near UV photons; right: MWPC data, far UV photons.

The effects of the pressure and of the temperature gradients inside the RICH-1 vessel are negligible.

The refractive indexes are experimentally determined at fixed time intervals (namely every 24 h of data taking) and then the evolution of the index value is calculated as a function of the pressure and of the temperature of the radiator, which are continuously monitored.

8. The angular resolution

8.1. The Θ_{PHOTON} resolution

 σ_{θ} is the error associated to the reconstructed Cherenkov photon angle θ . It depends on the photon detector type (Section 2). The padsizes lead to a geometrical contribution to σ_{θ} of approximately 1 mrad for MAPMTs and 0.7 mrad for MWPCs. For the MAPMTs, the geometrical contribution has to be folded with the dispersion due to the chromaticity of the lens telescope in front of the MAPMTs. The total error from the position measurement is 1.6 mrad.

Moreover the photons undergo the chromatic dispersion: this dispersion is larger for the photons detected by the MAPMTs than for the photons detected in the MWPCs because of the different sensitivity to the photon wavelengths (Fig. 3). It is 0.9 and 0.6 mrad respectively.

The spherical aberrations due to the reflection by the spherical mirror surfaces also contribute to the dispersion of the photon angle with respect to the angle of emission. This effect is strongly position dependent. The mean contribution in the central region is 0.7 mrad, in the peripheral region it is 1.7 mrad.

Other contributions to the dispersion come from the errors affecting the reconstructed particle trajectory and momentum, the nonzero magnetic field in the radiator volume, the multiple scattering, the mirror imperfections and the alignment errors. In particular, two contributions are more relevant in the peripheral region. The particle momentum is more poorly determined: particles at large angles are analysed by the first COMPASS spectrometer only, while forward scattered particles are analysed by both spectrometers [6].

Moreover, for the very external mirror elements of the mirror walls the accuracy of the alignment procedure is decreased due to the limited statistics. Globally, these contributions account for 0.6 mrad for the central region and 1.3 mrad in the peripheral region.

 σ_{θ} is evaluated from the data; two different distributions are used: the distribution of the difference $\theta-\Theta_{\pi}$, assuming the π mass, for all the photons of a particle or the distribution of the difference $\theta-\Theta_R$.

 $\theta-\Theta_\pi$ has a clearer physical definition, but Θ_π depends on the uncertainties in the determination of the refractive indexes and the particle momentum.

These distributions, for both the detector types, are parametrised as a function of the particle polar angle Θ_P , the particle momentum and the photon azimuthal angle φ .

 σ_{θ} is given as a function of these parameters for two algorithms: in the likelihood based PID (Section 3.1), σ_{θ} is a function of the detector type, Θ_P and φ , while for ring recognition (Section 4.1), σ_{θ} is averaged over φ .

In Fig. 13 the distributions of $\theta-\Theta_\pi$ is shown. For the central region, data before and after the upgrade collected by MWPCs and MAPMTs respectively are presented. The peripheral region was poorly populated before the upgrade, as the whole COMPASS spectrometer acceptance has been enlarged from 2006 on. Comparing central region data, two features are remarkable: the improved signal over background level, thanks to the very low electronic noise of the MAPMTs

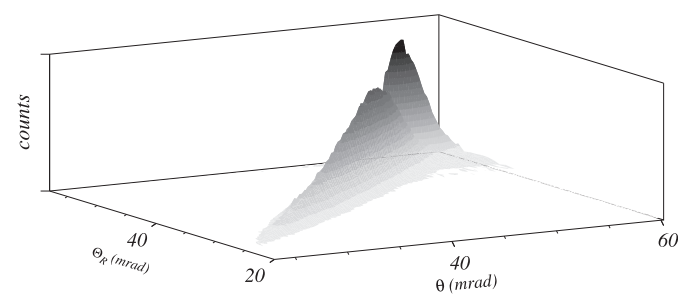


Fig. 14. The distribution of θ versus Θ_R .

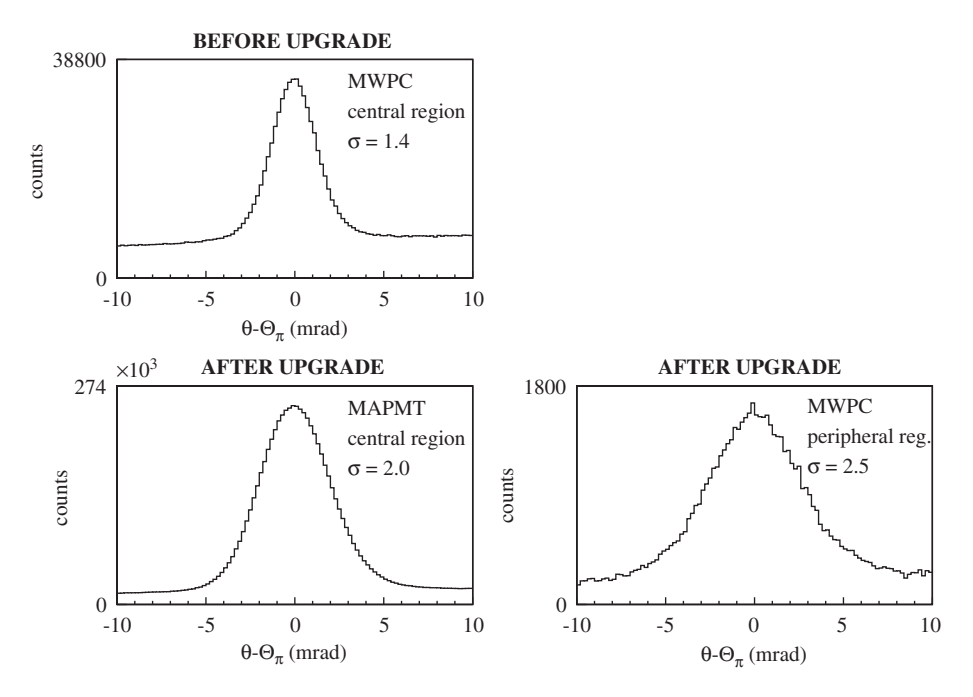
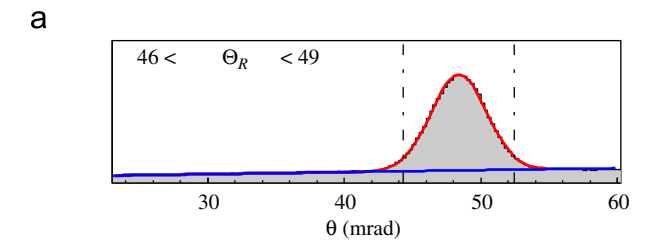


Fig. 13. Typical $\theta - \Theta_{\pi}$ distribution for *rings* entirely included in a single photon detector frame. Upper line, data collected before the implementation of the RICH upgrade, central region equipped with MWPCs. Lower line, data collected after the implementation of the RICH upgrade; left, central region equipped with MAPMTs; right: peripheral region equipped with MWPCs.

and their excellent time resolution, and the superior resolution for single photon detection of the MWPCs, mainly thanks to the smaller pad-size. The increased number of photons detected by the MAPMTs compensates for the reduced resolution (Sections 8.2 and 8.3). The worse resolution in the peripheral region is mainly due to the spherical aberration and the poorer particle momentum resolution.



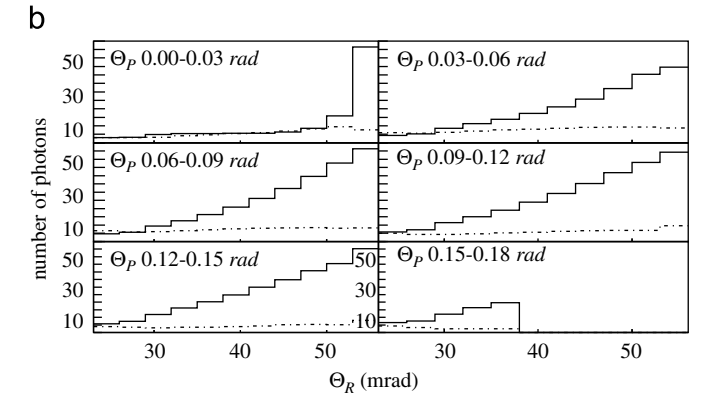


Fig. 15. Extraction of the number of *signal* photons per ring. The procedure is illustrated using MAPMT data. (a) Example of the θ distribution in a 3 mrad wide Θ_R band (from the two-dimensional plot of Fig. 14). The solid line is the best fit obtained with a Gaussian peak (signal) plus a quadratic form (background). (b) Summary of the extracted average number of photons per ring as a function of the ring angle for different values of the particle polar angle. The solid line corresponds to the *signal* photons, the dashed line to the *background* photons.

8.2. The number of photons

The number of detected Cherenkov photons per particle is evaluated from the data, separately for the two detector types.

The distribution of θ (Fig. 14) as a function of Θ_R (Section 6), for all the *photons* correlated to each particle, for all events, has been studied in bands of Θ_R , 3 mrad wide. For each band (Fig. 15(a)) the Cherenkov photons, emitted by that particle, cluster around Θ_R allowing to separate the signal from the background by means of a fit to the peak using a Gaussian plus a quadratic form. The average number of photons per *ring* is thus extracted as a function of the particle Cherenkov angle.

The results are summarised in Fig. 15(b) for the MAPMT photon detectors. The average number of photons N_S at saturation ($\beta \rightarrow 1$) is about 56 for the MAPMTs and 14 for the MWPCs, corresponding to a value of the detector response parameter N_0 (defined in Ref. [20]) of 70 and 16 cm⁻¹ respectively.

8.3. The Θ_{RING} resolution

A useful quantity to estimate the RICH resolution is σ_{Θ_R} , the error in the determination of the *ring* angle.

Statistically, in the absence of background, σ_{Θ_R} should be $\sigma_\theta/\sqrt{N_S}$, depending on the number of signal photons in the *ring*. σ_{Θ_R} is determined from the data; it is estimated as the standard deviation of a Gaussian fit to the distribution of the difference $\Theta_R-\Theta_\pi$, assuming the π mass.

The ring resolution extracted from the data is shown in Fig. 16, separately for the central region, data before and after the upgrade collected by MWPCs, and MAPMTs. The width of the distribution of $\Theta_R-\Theta_\pi$ gives a ring resolution $\sim 0.4, \sim 0.3$ and ~ 1.6 mrad respectively. Assuming the measured value of σ_θ (Section 8.1) and of N_S (Section 8.2), for the central region we obtain $\sigma_\theta/\sqrt{N_S}\simeq 0.37$ mrad before the upgrade and ~ 0.27 mrad after. No simple scaling is possible in the peripheral region, mainly populated by low momentum particles: these Cherenkov images are formed by a smaller number of photons.

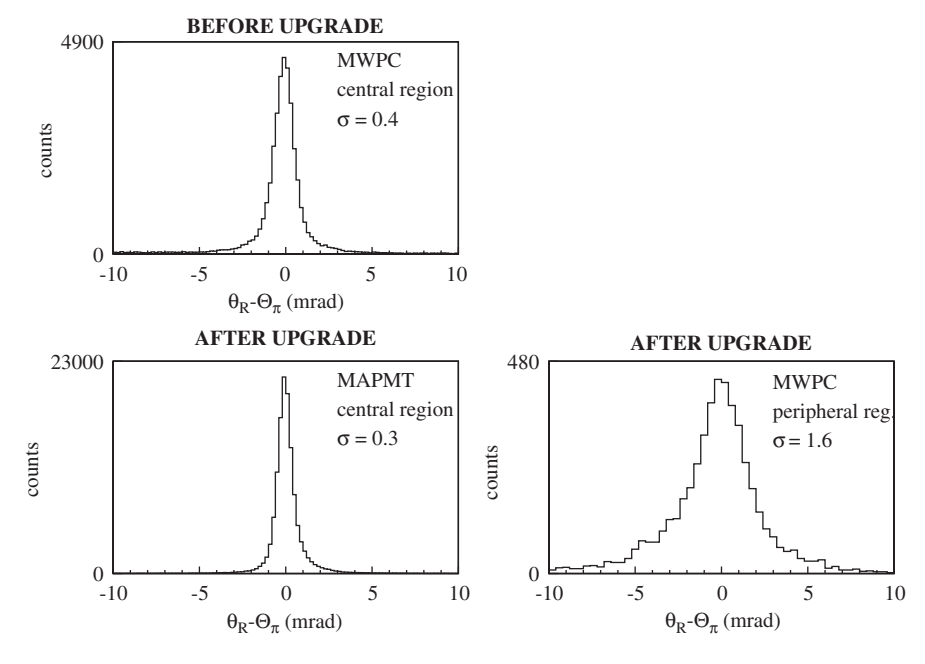


Fig. 16. $\Theta_R - \Theta_\pi$ distributions for *rings* entirely included in a single photon detector frame. Upper line, data collected before the implementation of the RICH upgrade, central region equipped with MWPCs. The typical measured resolution is 0.4 mrad. Lower line, data collected after the implementation of the RICH upgrade; left, central region equipped with MAPMTs, the typical measured resolution is 0.3 mrad; right: peripheral region equipped with MWPCs, the typical measured resolution is 1.6 mrad.

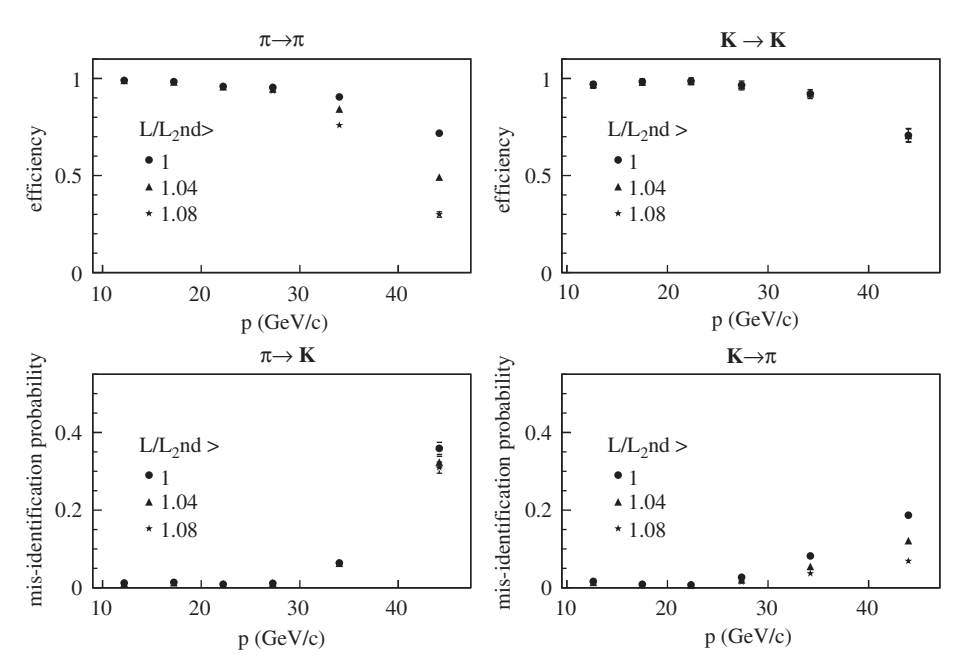


Fig. 17. Identification efficiency and mis-identification probability as a function of the particle momentum. Top left: identification of π as π ; top right: K as K; bottom left: π as K and bottom right: K as π . Each data set corresponds to a different cut applied to the ratio $\mathcal{L}/\mathcal{L}_{2nd}$.

9. PID efficiency and purity

9.1. PID cuts

As seen in Section 5, the likelihood function is evaluated for different mass hypotheses and for the background hypothesis. A first simple identification is done by choosing among the hypotheses the one corresponding to the highest value of the likelihood, \mathcal{L} . The identification purity can be improved by requiring the ratio of the likelihood with respect to the background hypothesis, \mathcal{L}_{back} or to the second highest likelihood \mathcal{L}_{2nd} to be above a certain threshold. For this purpose the two distributions $\mathcal{L}/\mathcal{L}_{\textit{back}}$ and $\mathcal{L}/\mathcal{L}_{\textit{2nd}}$ are considered. The former variable gives the quality of the separation between a mass hypothesis and the background hypothesis; if this variable is near 1, the distinction between particle and background hypothesis is ambiguous. In the same way, the latter variable indicates the distinction between two different mass hypotheses; this cut is adopted in order to have cleaner samples at high momenta, where the Cherenkov angles for different mass hypotheses, and consequently the likelihood values, are very close. Efficiency and purity depend strongly on the chosen cuts, as we will see in the next sections. The threshold for these cuts are usually tuned for the specific analysis to find a good compromise between the efficiency and the purity of the sample.

9.2. The PID efficiency

The PID efficiency is defined as the ratio between the number of particles correctly identified and the total number of particles of a pure sample.

The PID efficiency has been determined for pions (kaons), using as a sample the pions (kaons) from the $K_{5}^{0}(\phi_{1020})$ decay into two charged particles. The sample has been built by selecting pairs of charged hadrons with the correct charge assignment and invariant mass of the parent particle. The efficiency is defined as the ratio of the number of the correctly identified particles over the population of the mass peak. It is possible to define the mis-identification

probability as the ratio of the number of events of the peak for which one particle is wrongly identified divided by the number of events in the peak.

Due to different background level and to the fact that the Cherenkov angle saturates with the increasing momentum, the efficiency of the detector shows a dependency on the phase space. In Fig. 17 the efficiency and the mis-identification probability are shown for pions and kaons as a function of momentum and for three different cuts applied to the ratio $\mathcal{L}/\mathcal{L}_{2nd}$.

The identification efficiency for momenta below $30\,\text{GeV}/c$, where the expected Cherenkov angles for the different mass hypotheses are well separated, is above 90% both for kaons and for pions. As the Cherenkov angle saturates, the identification efficiency decreases and the mis-identification probability increases. Increasing cuts applied to the ratio $\mathcal{L}/\mathcal{L}_{2nd}$ decreases the mis-identification probability, making the sample purer, but at the same time reduces the identification efficiency.

9.3. The sample purity

While the efficiency is a property of the detector itself, the purity depends also on the different population of the particle types. Being the pion contribution the dominant one, the purity of the kaon sample is the main issue.

The purity can be extracted from real data considering the relation between the number of identified hadrons, $N_{\pi,K}^I$, and true hadrons, $N_{\pi,K}^T$.

$$\begin{pmatrix} N_{\pi}^{I} \\ N_{K}^{I} \end{pmatrix} = \begin{pmatrix} P(\pi \to \pi) & P(K \to \pi) \\ P(\pi \to K) & P(K \to K) \end{pmatrix} \cdot \begin{pmatrix} N_{\pi}^{T} \\ N_{K}^{T} \end{pmatrix}$$
(4)

in which the diagonal terms in this matrix of identification are the RICH-1 efficiencies and the off-diagonal terms are the mis-identification probabilities, that are evaluated from the data as described in Section 9.2.

⁴ The proton contribution is neglected in the following.

The purity of the kaon sample is evaluated as the ratio of the number of true kaons in the identified kaon sample to the total number of particles identified as kaons:

$$Purity(K) = \frac{P(K \to K) \cdot N_K^T}{N_K^I}.$$
 (5)

In Eq. (5), N_K^I is known directly from the data after the identification procedure; the term N_K^T is evaluated from the matrix coefficients and the number of identified particles, inverting Eq. (4). The same procedure can be applied to evaluate the pion purity.

To take into account the fact that the RICH-1 efficiencies depend very much upon the hadron phase space (Section 9.2), the matrix of identification is evaluated as a function of the particle momentum.

The purities calculated for a K sample selected from standard COMPASS deep inelastic scattering events are shown in Fig. 18 as a function of the particle momentum. The different sets of data points correspond to different cuts applied to the variable $\mathcal{L}/\mathcal{L}_{2nd}$: in the momentum range up to 30 GeV/c the purities are above 90%, for all the cuts shown. The difference between the selections is relevant at higher momenta, where the more restrictive cuts allow to reach purities around 80%.

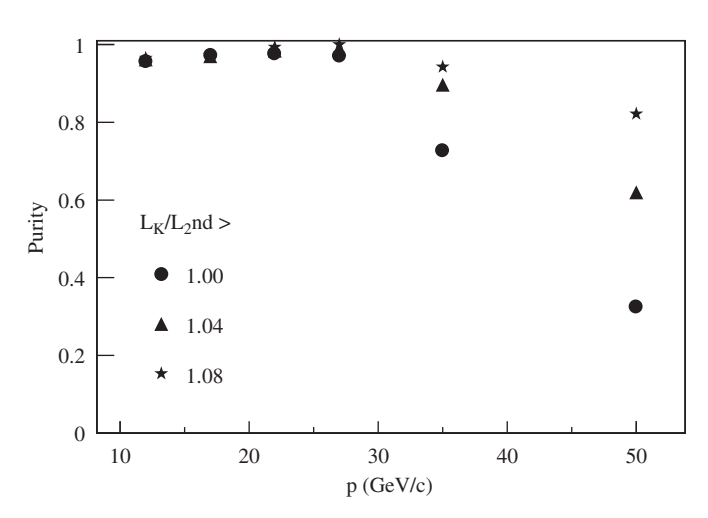


Fig. 18. Purity of K sample as a function of the particle momentum. Different data sets correspond to different cuts on the variable $\mathcal{L}/\mathcal{L}_{2nd}$.

9.4. PID below Cherenkov threshold

RICH-1 is extensively used also to identify hadrons with momentum below their Cherenkov thresholds; the identification relies on the absence of Cherenkov photons emitted from the particle. Two different signatures are possible: in the simplest case, the particle track goes through the RICH acceptance but no photons are detected in the fiducial region used to compute the likelihood. In more complex situations, for example in events with several reconstructed tracks, the region can contain uncorrelated photons: in this case the track is identified as a particle below threshold if the background likelihood is the highest one. This identification below threshold is effective only if the efficiency for the positive PID is high. This recipe has been applied to the identification of the kaons with momentum below 9 GeV/c from the ϕ decay: an efficiency larger than 90% has been found. Being the proton contribution negligible in this sample, the mis-identification rate is equivalent to the inefficiency of pion identification in the corresponding momentum range, namely less than 5%.

Furthermore, for particles below their threshold RICH-1 can be used as a veto. If the particle is positively identified as a mass above threshold, it is rejected.

10. The RICH-1 role in COMPASS analysis

The relevance of the hadron identification for the COMPASS physics programme has already been recalled (Section 1). The good performance of the PID is mandatory for the measurement of the gluon polarisation from the photon–gluon fusion with open charm

Table 1

Values of signal over background (S|B) and signal times the purity of the peak $(S^2|S+B))$ evaluated in a region of $\pm 2\sigma$ around the D^0 mass peak, both for the old and the upgraded RICH-1 (data taken from the COMPASS Collaboration in 2004 and 2006 respectively). The values are reported for the mass spectrum without and with PID; in the last column the ratio between these quantities is shown. *Courtesy of COMPASS Collaboration*.

		no PID	PID	PID/no PID
RICH before upgrade	S/B $S^2/(S+B)$	0.19	1.93	10
(2004 data)		437	1632	3.7
Upgraded RICH	S/B	0.11	1.87	17
(2006 data)	$S^2/(S+B)$	274	1907	7

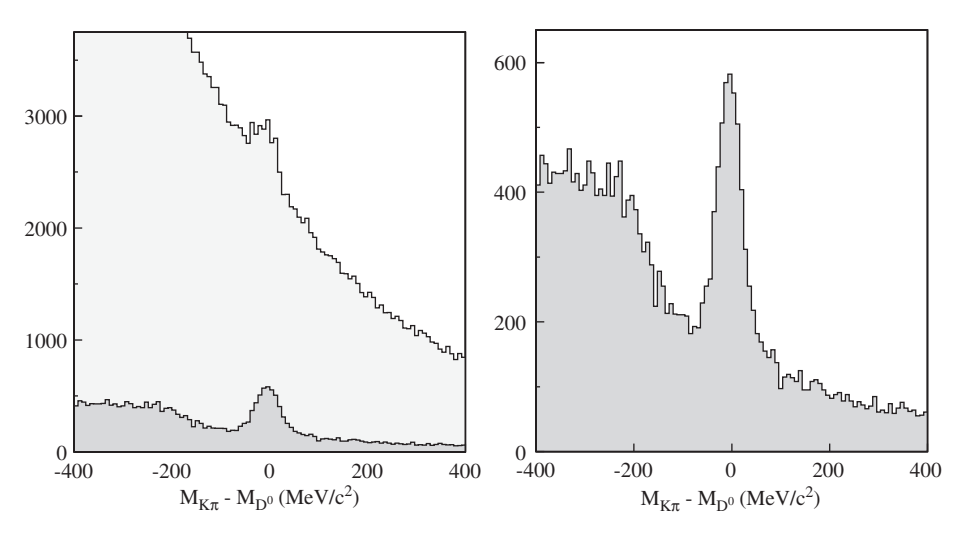


Fig. 19. Difference of the π K invariant mass and the D^0 mass, data taken in 2006 by the COMPASS Collaboration. Left: spectra without (light grey) and with (dark grey) PID. Right: zoom of the spectrum with PID. *Courtesy of the COMPASS Collaboration*.

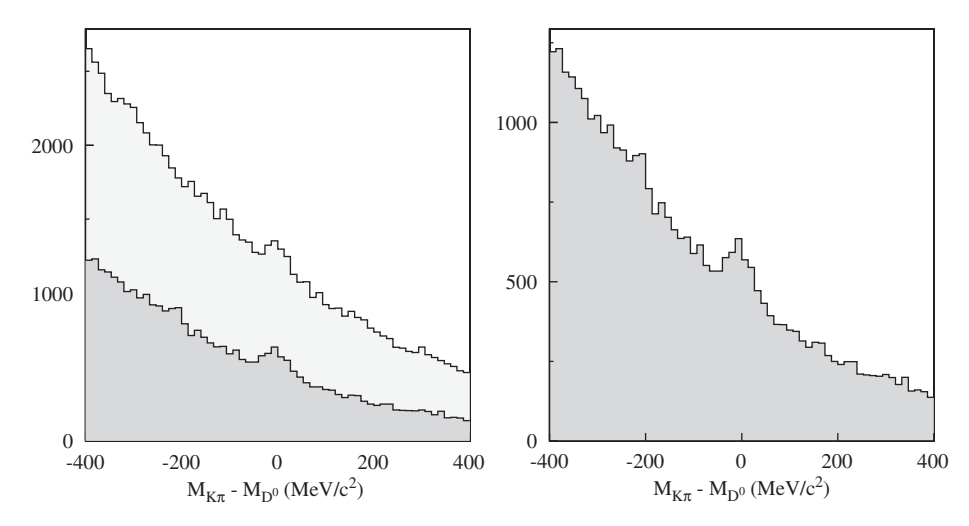


Fig. 20. Difference of the π K invariant mass and the D^0 mass, data taken in 2006 by the COMPASS Collaboration. Left: spectra without (light grey) and with (dark grey) the identification of the kaon below threshold. Right: zoom of the spectrum with PID. *Courtesy of the COMPASS Collaboration*.

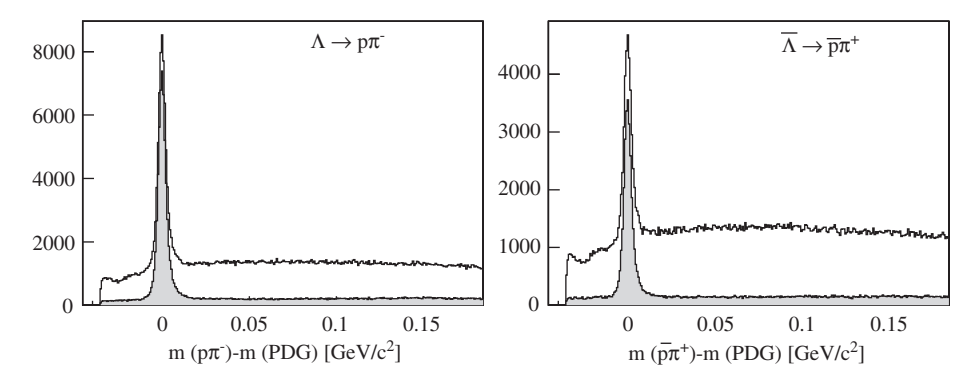


Fig. 21. Λ and $\overline{\Lambda}$ mass spectra without (white) and with (grey) the identification of the decay proton or antiproton with the RICH-1. Courtesy of the COMPASS Collaboration.

production in the final state [5]. Particle identification is a key ingredient also in the analysis of many other physics channels such as the extraction of the flavor separated helicity PDFs [4], the Collins and Sivers asymmetries of pion and kaons [3] and a clean selection of the Lambda sample.

The open charm reaction is identified by looking for D⁰ production. The D mesons are selected through their decays in the two channels: $D^* \to D^0 \pi^+_{slow} \to K^- \pi^+ \pi^+_{slow}$ ("D* sample") and $D^0 \to K^- \pi^+$ ("D0 sample"), and their charge conjugates. In order to reduce the large combinatorial background, RICH-1 is used to identify the K and the π from the D⁰ decay. For the identification of slow pions in the D* channel, RICH-1 is used as a veto requiring the track not to be identified as an electron (Section 9.4). For the D* sample, the difference of the πK invariant mass and the D⁰ mass is shown in Fig. 19, for data taken by the COMPASS Collaboration in 2006, when the RICH was in its upgraded version. The figure illustrates the huge reduction of the combinatorial background given by the particle identification. The values of signal over background (S/B) and signal times the purity of the peak ($S^2/(S+B)$), a quantity that is inversely proportional to the square of the statistical error of the measurement, are shown in Table 1. The values have been evaluated in a region of $\pm 2\sigma$ around the D⁰ mass, for the selection without and with PID, and for both the old and upgraded RICH (data from 2004 and 2006 respectively). Already before the RICH upgrade, the PID allows to improve the S/B and $(S^2/(S+B))$ by a factor 10 and 3.7 respectively. A further improvement comes from the RICH upgrade: the S/B ratio increases to 17, while the $S^2/(S+B)$ to 7, despite the larger combinatorial background in the 2006 data, given by the larger acceptance of the apparatus thanks to the new target solenoid [6].

The D^0 s have been selected also by identifying the K below Cherenkov threshold, in the momentum range between the pion and the kaon Cherenkov thresholds (Section 9.4). The D^0 mass spectrum obtained from the 2006 data is shown in Fig. 20, together with the spectrum without PID applied; the values of the ratios S/B and $S^2/(S+B)$ after applying the PID increase by a factor three and four, respectively.

The RICH PID has been used also to select the Λ and $\overline{\Lambda}$ barions, which are usually tagged by searching for the dominant decay channel into π^-p and $\pi^+\overline{p}$ respectively. Due to the high Cherenkov threshold for the proton, the RICH is used as a veto excluding the other mass hypotheses (Section 9.4). As an example, Fig. 21 shows the selection of the Λ and $\overline{\Lambda}$, without and with PID, as done in the analysis of the Λ transverse polarisation. It can be noted that the RICH identification increases considerably the purity of the Λ and $\overline{\Lambda}$ sample, of a factor 6 and 7 respectively, with a small loss in statistics, below 3%.

11. Conclusions

This article, dedicated to the software package RICHONE developed for COMPASS RICH-1 and to the detector performance extracted using the package itself, completes a detailed description of the RICH-1 detector in its upgraded version; the detector design and the hardware aspects have been described elsewhere [8,9].

The RICH-1 contribution to the physics results of the COMPASS experiment is essential, as illustrated, for instance, by the clean detection of the D⁰ mesons via their decay products, a difficult task

when performed with a setup where a micro-vertex detector cannot be used, as it is the case for COMPASS, due to the use of a solid state polarised target.

The excellent performance obtained could be reached thanks to the combination of several ingredients, namely a careful detector design, an accurate construction, where all the components have received great attention, and powerful software tools. An important aspect has been the parallel development of the hardware and software elements, with continuous feedback from both sides. We believe that such a synergistic attitude has been essential in obtaining the performance described in this article.

Acknowledgements

The authors are grateful to the colleagues of the COMPASS Collaboration for constant support and help. This work was supported in part by the BMBF (Germany), by MEYS (Czech Republic), grant LA08015, by the FCT (Portugal), and the European Community-research Infrastructure Activity under the FP6 programme (Hadron Physics, RII3-CT-2004-506078).

References

- [1] The COMPASS Collaboration, Proposal, CERN/SPSLC/96-14, SPSC/P297, addendum, March 1, 1996, CERN/SPSLC/96-30, SPSLC/P297, addendum 1, May 20,
- [2] E.S. Ageev, et al., COMPASS Collaboration, Phys. Lett. B 612 (2005) 154; V.Yu. Alexakhin, et al., COMPASS Collaboration, Phys. Rev. Lett. 94 (2005) 202002
 - E.S. Ageev, et al., COMPASS Collaboration, Eur. Phys. J. C 41 (2005) 469:

- E.S. Ageev, et al., COMPASS Collaboration, Phys. Lett. B 633 (2006) 25; V.Yu. Alexakhin, COMPASS Collaboration, Phys. Lett. B 647 (2007) 8; E.S. Ageev, et al., COMPASS Collaboration, Nucl. Phys. B 765 (2007) 31; V.Yu. Alexakhin, COMPASS Collaboration, Phys. Lett. B 647 (2007) 330: M. Alekseev, et al., COMPASS Collaboration, Eur. Phys. J. C 52 (2007) 255; M. Alekseev, et al., COMPASS Collaboration, Phys. Lett. B 660 (2008) 458; M. Alekseev, et al., COMPASS Collaboration, Eur. Phys. J. C 64 (2009) 171; A. Alekseev, et al., COMPASS Collaboration, Phys. Rev. Lett. 104 (2010) 241803; M.G. Alekseev, et al., COMPASS Collaboration, Phys. Lett. B 690 (2010) 466; M.G. Alekseev, et al., COMPASS Collaboration, Phys. Lett. B 692 (2010) 240; M.G. Alekseev, et al., COMPASS Collaboration, Eur. Phys. J. C 70 (2010) 39; M.G. Alekseev, et al., COMPASS Collaboration, Phys. Lett. B 693 (2010) 227.
- M. Alekseev, et al., COMPASS Collaboration, Phys. Lett. B 673 (2009) 127.
- [4] M. Alekseev, et al., COMPASS Collaboration, Phys. Lett. B 680 (2009) 217.
- M. Alekseev, et al., COMPASS Collaboration, Phys. Lett. B 676 (2009) 31.
- [6] P. Abbon, et al., COMPASS Collaboration, Nucl. Instr. and Meth. A 577 (2007) 455.
- E. Albrecht, et al., Nucl. Instr. and Meth. A 553 (2005) 215 and references therein.
- [8] P. Abbon, et al., Nucl. Instr. and Meth. A 616 (2010) 21. [9] P. Abbon, et al. Nucl. Instr. and Meth. A 587 (2008) 371.
- [10] J. Engelfried, et al., Nucl. Instr. and Meth. A 431 (1999) 53.
- [11] H.W. Siebert, et al., Nucl. Instr. and Meth. A 343 (1994) 60. [12] N. Akopov, et al., Nucl. Instr. and Meth. A 479 (2002) 511.
- [13] E. Albrecht, et al., Nucl. Instr. and Meth. A 502 (2003) 266.
- [14] E. Albrecht, et al., Nucl. Instr. and Meth. A 502 (2003) 236.
- [15] RD26 collaboration, Status Reports: CERN/-DRDC 93-36, 94-49, 96-20; The ALICE collaboration, Technical Design Report of the High Momentum Particle Identification Detector, CERN/LHCC 98-19, ALICE TDR 1, 14 August, 1998; F. Piuz, Nucl. Instr. and Meth. A 502 (2003) 76.
- [16] C. Santiard, et al., Gassiplex: a low noise analog signal processor for readout of gaseous detectors, Presented at the Sixth Pisa Meeting on Advanced Detector, La Biodola, Isola d'Elba, Italy, May 1994.
- [17] P. Abbon, et al., Nucl. Instr. and Meth. A 567 (2006) 104.
- [18] M.J. French, et al., Nucl. Instr. and Meth. A 466 (2001) 359.
- [19] E. Albrecht, et al., Nucl. Instr. and Meth. A 456 (2001) 190 private communication by E. Fokitis.
- [20] T Visilantis I Seguinot Nucl Instr and Meth A 343 (1994) 30
- [21] R.J. Barlow, Nucl. Instr. and Meth. A 297 (1990) 496.